AGU PUBLICATIONS

JGR

Journal of Geophysical Research: Solid Earth

RESEARCH ARTICLE

10.1002/2013JB010559

Key Points:
- USArray provides enough *Sn* data to image *Vp/Vs* structure in the mantle lid
- We are unable to resolve shear wave splitting directly in *Sn* waveforms
- *Pn* and *Sn* time terms provide constraints on crustal thickness and velocity

Correspondence to:
J. S. Buehler,
jsbuehle@ucsd.edu

Citation:
Buehler, J. S., and P. M. Shearer (2014), Anisotropy and *Vp/Vs* in the uppermost mantle beneath the western United States from joint analysis of *Pn* and *Sn* phases, *J. Geophys. Res. Solid Earth*, *119*, doi:10.1002/2013JB010559.

Received 26 JUL 2013
Accepted 19 JAN 2014
Accepted article online 27 JAN 2014

Anisotropy and *Vp/Vs* in the uppermost mantle beneath the western United States from joint analysis of *Pn* and *Sn* phases

J. S. Buehler[1] and P. M. Shearer[1]

[1]Scripps Institution of Oceanography, University of California, San Diego, La Jolla, California, USA

Abstract *Pn* and *Sn* phases are valuable for resolving velocity structure in the mantle lid, as they propagate horizontally right below the Moho. Relatively few *Sn* tomography attempts have been made compared to *Pn*, because *Sn* is often highly attenuated or buried in *P* wave coda. USArray has greatly increased data coverage for regional phases, and both *Pn* and *Sn* are routinely picked by network analysts. Here we jointly invert *Pn* and *Sn* arrival time residuals with a modified time-term analysis and a regularized tomography method and present new maps of crustal thickness, uppermost mantle *P* velocity perturbations, *Vp/Vs* ratios, and azimuthal anisotropy strength and orientation beneath the western United States. The results indicate partially molten mantle below the Snake River Plain and the Colorado Plateau. The seismic structure of the top ~40 km of the mantle below the Colorado Plateau differs from that seen at greater depths in other studies, such as surface wave or teleseismic body wave tomography, whereas the Snake River Plain anomaly just below the Moho is comparable to structures seen at about ~200 km depth. *Pn* fast axes provide complementary information to *SKS* shear wave splitting observations, and our analysis indicates that in several regions in the western United States the orientation of azimuthal anisotropy changes with depth in the upper mantle. However, we have so far been unable to resolve shear wave splitting directly in *Sn* waveforms, which seem to be dominated by *Sn-SV* energy.

1. Introduction

The North American lithosphere and upper mantle has attracted much recent attention, as the increased data coverage from USArray has allowed imaging its seismic structure on a regional scale. Seismic velocities in the upper mantle are generally lower in the tectonically active western United States and higher below the Great Plains province (Figure 1a), but many smaller-scale anomalies appear in recent tomographic maps, such as lithospheric drip features or downwellings imaged with body wave tomography [e.g., *Obrebski et al.*, 2011; *Roth et al.*, 2008; *Schmandt and Humphreys*, 2010; *West et al.*, 2009]. In addition, complex patterns of azimuthal anisotropy have been imaged in great detail in both the crust and upper mantle in the western United States with new ambient noise tomography methods [e.g., *Lin and Ritzwoller*, 2011; *Lin et al.*, 2011; *Ritzwoller et al.*, 2011] and with shear wave splitting analysis [e.g., *Liu*, 2009; *West et al.*, 2009]. Crustal thickness estimates have been made with various approaches on local and regional scales, including receiver function analysis [*Gilbert*, 2012; *Lowry and Perez-Gussinye*, 2011; *Levander et al.*, 2011] and *Pn* tomography [*Buehler and Shearer*, 2010]. Recently, *Tape et al.* [2012] compiled a variety of studies to obtain a detailed Moho surface for California.

However, even with improved resolution, interpretation of imaged seismic anomalies remains challenging, as the seismic velocities are influenced by a variety of factors, including temperature, composition, the presence of partial melt or water, and, in some studies, unmodeled anisotropy [e.g., *Goes et al.*, 2000; *Perry et al.*, 2006]. In addition, surface wave tomography averages over the crust and upper mantle, depending on frequency, and teleseismic body wave tomography with near-vertical incidence angles typically has low vertical resolution in the lithosphere. Joint surface and body wave tomographies have been successful at mitigating the problem [*Obrebski et al.*, 2011]. Recently, *Shen et al.* [2013] jointly inverted receiver functions and surface wave dispersion to increase vertical resolution. Seismic velocity and anisotropy imaged with *Pn* and *Sn* waves, which are confined to the mantle lid, can provide effective additional depth constraints.

Pn and *Sn* are regional seismic phases that propagate horizontally in the uppermost mantle just below the Moho and are the first-arriving *P* and *S* phases at regional distances. They are typically described as critically

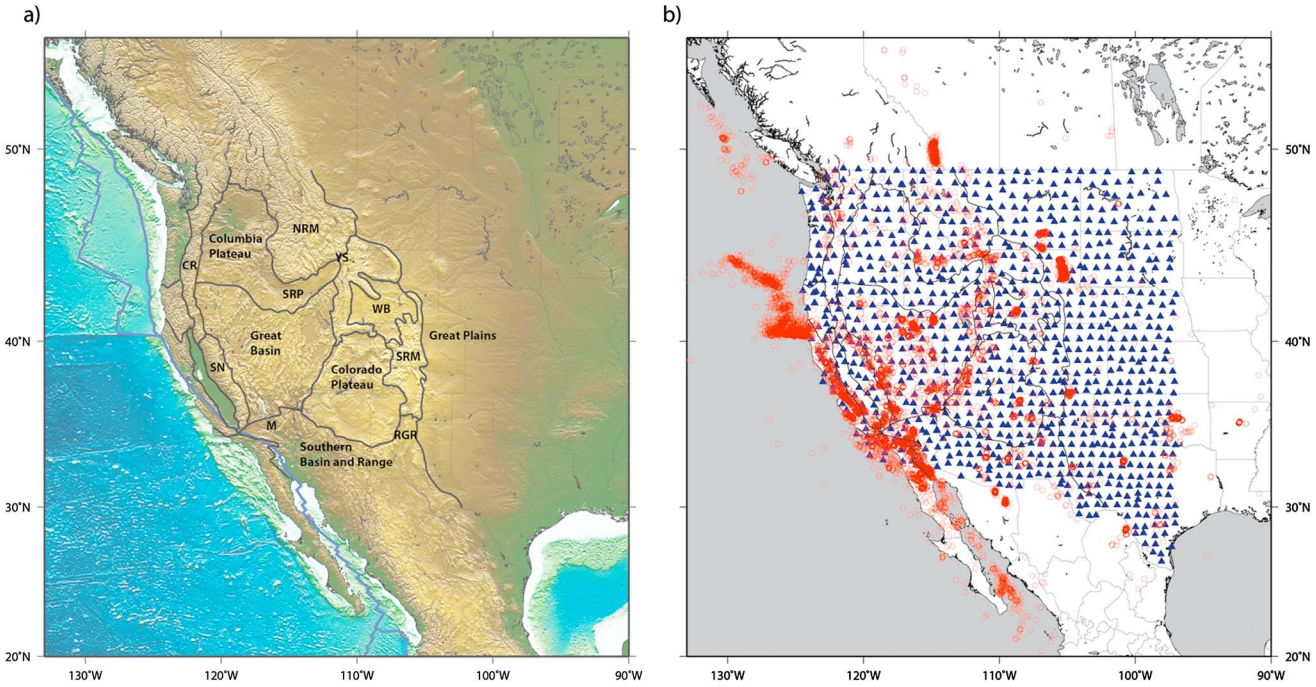

Figure 1. (a) Overview map of study region with physiographical provinces indicated by black lines and names. The abbreviations are in place for the Cascade Range (CR), Sierra Nevada (SN), Mojave (M), Snake River Plain (SRP), Northern Rocky Mountains (NRM), Yellowstone (YS), Wyoming Basin (WB), Southern Rocky Mountains (SRM), and Rio Grande Rift (RGR). (b) USArray transportable array stations (blue triangles) and events (red circles) used in this study.

refracted or head waves along the Moho, although effects from uppermost mantle velocity gradients, lateral velocity heterogeneities, and Moho topography contribute to more complicated propagation characteristics [e.g., *Bakir and Nowack*, 2012]. However, *Langston* [1982] found that *Pn* can be well modeled as a head wave in the western United States. Since *Pn* and *Sn* tomographic studies are dependent on event-station distances between ~2 and ~14°, depending on crustal thickness and mantle lid structure, USArray has greatly increased usable data outside the westernmost regions of North America and permits imaging *Pn* and *Sn* velocity structure with good resolution on a regional scale.

Regional phases are challenging to analyze, especially in a tectonically active region like the western United States, since they are strongly affected by heterogeneities in the uppermost mantle, and *Sn* is often highly attenuated [e.g., *Beghoul et al.*, 1993]. *Chulick and Mooney* [2002] compiled *Pn* and *Sn* studies for North America to produce contour maps of the seismic velocity in the uppermost mantle. They found only 114 *Sn* data points for the continent and could only produce a very rough *Sn* velocity map with generally lower velocities in the west, and higher velocity beneath the Great Plains. Therefore, the increased *Sn* observations with USArray are valuable to gain further insight into the seismic properties of the mantle lid. Often anomalous velocity structures of regional phases are interpreted with respect to the thermal structure of the lithosphere, as temperature seems to be the dominant factor influencing seismic velocities [*Goes et al.*, 2000]. Jointly analyzing *Pn* and *Sn* data, and imaging the *P*-to-*S* velocity ratio (*Vp*/*Vs*), can help identify regions where properties other than temperature influence seismic velocities, because the *P* and *S* waves generally have different sensitivities to the parameters that influence seismic velocities.

Anisotropy that is not accounted for in inversions can map into spurious velocity anomalies, for example, in regions with a dominant ray direction. It is therefore critical to include anisotropy in upper mantle tomography. In addition, seismic anisotropy can be related to the mantle strain history [e.g., *Long and Becker*, 2010; *Park and Levin*, 2002; *Savage and Silver*, 1993], and it seems especially important to put *Pn* and *Sn* anisotropy models into the context of measurements from surface wave tomography and shear wave splitting, which have lower vertical resolution but little trade-off with lateral heterogeneities, in order to compare the anisotropic observations to predictions from geodynamic models. We previously found that *Pn* anisotropy differs from recent shear wave splitting results [*Buehler and Shearer*, 2010], suggesting that the distinct rotational fast axis around the Great Basin seen in splitting studies originates from sublithospheric mantle

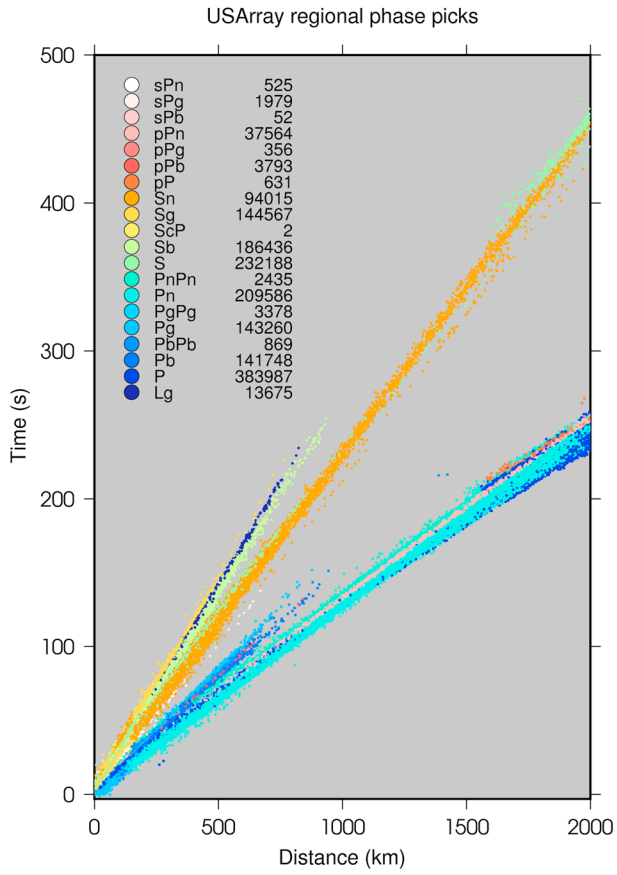

Figure 2. Regional phase picks in the USArray data set recorded at stations with longitude >97°W between April 2004 and June 2012. Number of picks according to the ANF tables is listed.

flow. To analyze the nature of uppermost mantle material more completely, it is useful to include shear wave arrivals. With *Pn* anisotropy alone we can only resolve three of the five parameters of the elastic tensor that describes a weakly hexagonal anisotropic material with a known horizontal symmetry axis, but with measurements of azimuthal velocity variations of *Pn*, *Sn-SH*, and *Sn-SV* velocities, it is possible, in theory, to estimate all five elastic parameters.

Only a few studies of uppermost mantle structure include the shear arrivals, even though *Pn* tomography exists for many regions, and usually they are addressed separately. Here we attempt joint *Pn-Sn* tomography for the western United States. We find some evidence for shear wave splitting in the *Sn* waves, and waveform stacks generally show that *Sn-SH* arrives before *Sn-SV* at large distances, but we are not able to successfully automate the analysis or to more locally resolve shear wave anisotropy. Still, we find useful signal in the *Sn* picks and extend our previous studies that used *Pn* data alone [*Buehler and Shearer*, 2010, 2012] to image *Vp/Vs* anomalies and improve our understanding of the imaged *Pn* velocity anomalies. In addition, we gain further constraints on crustal thickness and velocity structure from the set of *Sn* time terms that account for the time the rays spend in the crust.

2. Data and Methods

2.1. Regional Traveltime Picks

We use the regional uppermost mantle *Pn* and *Sn* phases recorded at USArray stations at −125° to −97° longitude from April 2004 to June 2012 (Figure 1b). *Sn* is often inefficient in propagation or buried in *P* wave coda, which makes picking difficult, and our attempt to use autopicker picks to fill in data gaps was mostly unsuccessful. We found, however, a number of *Sn* array network facility (ANF) analyst picks in the USArray data set. Analysts at the ANF routinely pick first arrivals and sometimes also later phases. Figure 2 provides an overview of the available regional picks according to the assigned labels for the stations and recording times we use here. There is some reason to doubt the *Sn* picks, as the phase is highly attenuated on paths in the western United States [*Beghoul et al.*, 1993]. However, we visually inspected many seismograms and performed stacking analysis to identify regions that transmit *Sn* and found that the highly attenuating regions are similar in size to the low-velocity anomalies. In addition, separate *Sn* tomography with the ANF analyst picks shows similar large-scale features as imaged with *Pn* data (see below) and demonstrates that these picks measure useful *Sn* signal.

All the arrival time picks that we are using here are available for download in monthly intervals at http://anf.ucsd.edu/tools/events/ (last accessed July 2013). We select earthquakes and quarry blasts from longitude −135°E to −90°E, and latitude 20° to 60°, and allow a maximum event depth of 30 km. We found that the ANF pick label is not always reliable and therefore restrict epicentral distances to be within 200 and 1400 km in order to avoid both crustal phases and rays sampling submantle-lid regions, respectively. Looking at

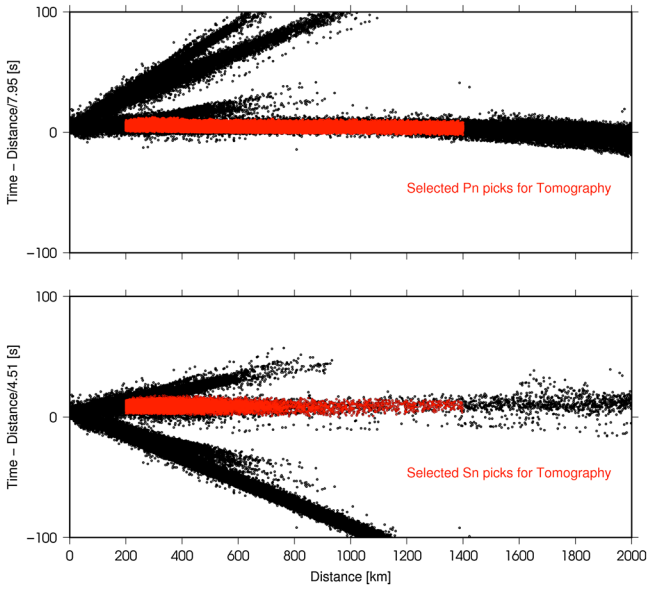

Figure 3. Time-distance plots of the regional arrival time picks and our windowed (top) *Pn* and (bottom) *Sn* picks that we are using in the tomography.

a reduced time-distance plot (Figure 3), the *Pn* picks form a straight line up to ~1400 km but start to bend at longer ranges, indicating that these waves probably dive beneath the mantle lid. The *Sn* arrivals form a fairly straight line, but there are many fewer picks at larger ranges. Next, we proceed in iterative fashion to window the arrivals in space and time, and require all stations to have at least five records and all events to be recorded with picks by at least five stations (three for *Sn*). In addition, we discard picks with residuals larger than 3 s (four for *Sn*) after a 1-D time-term fit. The final data set is indicated in red in Figure 3 and consists of ~183,000 and ~45,000 *Pn* and *Sn* picks, respectively, from 13,200 events recorded at 977 station locations.

2.2. Analysis of *Sn* Picks and Waveforms

Working with *Sn* is not only more challenging compared to *Pn* because of higher attenuation and typically lower signal-to noise ratios but also because shear wave behavior in anisotropic media is generally more complicated than that of compressional waves. However, it is worth the effort, in theory, to incorporate both the *P* and *S* waves together in order to obtain a more complete picture of the anisotropy in the uppermost mantle and to compare observations to model predictions for an improved understanding of the mantle strain history.

Seismic anisotropy manifests itself in seismic velocities that vary with azimuth and in split shear wave arrivals. Comparison of these anisotropic characteristics with elastic properties of upper mantle material provides information on the fabric and deformation of material at depth. *Moschetti et al.* [2010a] estimated relatively strong positive ($V_{SH} > V_{SV}$) azimuthally averaged radial anisotropy in the Basin and Range region in the uppermost mantle. We make similar path-averaged observations at large ranges in waveform stacks for the whole western United States region where we observe *Sn-SH* to arrive before *Sn-SV*. As previously discussed, *Pn* and surface wave tomographies also show considerable azimuthal anisotropy. In the upper mantle, anisotropy is thought to be mostly caused by lattice-preferred alignment of olivine crystals where the olivine *a* axis aligns with the direction of mantle flow. This introduces a form of anisotropy that is well modeled with hexagonal symmetry with a horizontal axis [e.g., *Christensen*, 1984; *Maupin and Park*, 2007].

To obtain wave speeds and polarizations of each quasi *P* and the two quasi *S* waves it is generally necessary to solve for the eigenvalues and vectors of the Christoffel equation, which gives the particle motions and velocities of plane waves in a medium with a given elasticity tensor for each propagation direction [e.g., *Babuska and Cara*, 1991]. It is simpler to study the azimuthal dependence on seismic velocities with approximations to the exact solution of the Christoffel equation, and for weakly anisotropic material, the anisotropy can be expressed as perturbations to the isotropic wave speeds [*Backus*, 1965; *Crampin*, 1981].

In a hexagonally symmetric material with a horizontal symmetry axis, the two quasi *Sn* waves are polarized *SH* and *SV*, and the azimuthal velocity variations can be expressed according to *Backus* [1965] as

$$V_P^2 = A + B\cos 2\theta + C\cos 4\theta$$
$$V_{SV}^2 = D + E\cos 2\theta$$
$$V_{SH}^2 = C + D + E - C\cos 4\theta$$

where θ is the angle from the symmetry axis. A, B, C, D, and E are related to the coefficients of the elastic tensor, and knowledge of these five parameters is enough to describe a hexagonally symmetric anisotropy. According to these equations, we could recover all five parameters needed if we can separately measure the velocities of *Sn-SH* and *Sn-SV*, and if the azimuthal coverage is acceptable. We could then compare these observations with elastic tensors used to model uppermost mantle material in order to understand the tectonic forces that cause the alignment of the olivine crystals [e.g., *Shearer and Orcutt*, 1986]. This idealized model predicts that *Sn* should exhibit shear wave splitting, with vertically polarized *Sn* exhibiting a 2θ azimuthal dependence and horizontally polarized *Sn* exhibiting a 4θ azimuthal dependence.

However, for reasons that we do not completely understand, this is not what we observe. Our *Sn* polarization analyses may be summarized as follows: First, we tried to obtain separate *SH* and *SV* picks. Because the *Sn* picks from the ANF do not indicate their polarity, we attempted to pick, cross-correlate, and separately realign the radial and transverse components of the *Sn* waveforms. However, we achieved little success, as *Sn* is generally only weakly visible across the array, and clean arrivals can only be observed for a few regions in the western United States. Polarization filtering based on particle motion linearity [e.g., *Jurkevics*, 1988] did not help, as it only improves the picking accuracy of the faster-traveling shear wave before the particle motion becomes elliptical.

Next we tried to focus on just a few localized regions with relatively uniform *Pn* anisotropy to avoid path averaging of azimuthal variations. Figure 4a shows the measured azimuthal velocity variations for *Pn* and *Sn* on both the radial and transverse components for a station subarray in California. The velocity and azimuth measurements are obtained as described in *Buehler and Shearer* [2012], by fitting interstation differential times for the apparent velocity and direction of the incoming wavefront. However, velocity variations for both *Sn-SH* and *Sn-SV* show a similar 2θ pattern to that seen for *Pn*, and we find no evidence for 4θ oscillations or diminished anisotropy in the velocity of the transversely polarized wave. It is possible that *SV* energy is leaking onto the transverse component or that the largest amplitude signal is not caused by material anisotropy, but by complexities of the Moho topography. A ridge-like Moho topography under the Sierra Nevada could possibly cause 2θ variations in apparent velocity and needs further investigation.

Figure 4b shows another station subarray example for northwestern Nevada, where *Pn* tomography and a surface wave model [e.g., *Lin et al.*, 2011] indicate consistent east-west to northeast-southwest fast axes, but *Sn* velocity measurements appear scattered without a clear azimuthal signal. In this case, the scatter probably arises from incoherent low-amplitude waveform cross correlations that are prone to cycle skipping. In some cases, however, inspection of individual waveforms showed evidence for splitting in this region, which motivated us to try another approach. We attempted to predict the delay time between the two shear waves at individual stations given our *Pn* anisotropy results and then to compare these predictions with the measured amount of delay from picks on both the transverse and radial component. However, this also did not yield coherent results. The low-amplitude arrivals are hard to pick consistently with autopickers and the character of the waveforms is quite variable across the western United States. The approaches mentioned here might work better in regions with clearer *Sn* arrivals as, for example, in the Great Plains.

Although we currently cannot clearly resolve *Sn* anisotropy in the western United States, there appears to be useful signal in the *Sn* picks, as stand-alone *Sn* tomography (discussed below) following the approach by *Hearn* [1996] shows consistent large-scale features similar to USArray *Pn* analysis for the same region [*Buehler and Shearer*, 2010]. Since we found 2θ variations, but no 4θ azimuthal changes, it is reasonable to assume that the analyst picks measure mostly *Sn-SV* arrival times.

2.3. *Pn-Sn* Joint Analysis

USArray *Pn* tomography alone reveals prominent uppermost mantle velocity features that correlate well with known active processes as, for example, the large slow velocity anomaly in the Snake River Plain leading to the Yellowstone hot spot. Our goal here is to add the *Sn* arrival time picks to constrain *Vp/Vs* structure,

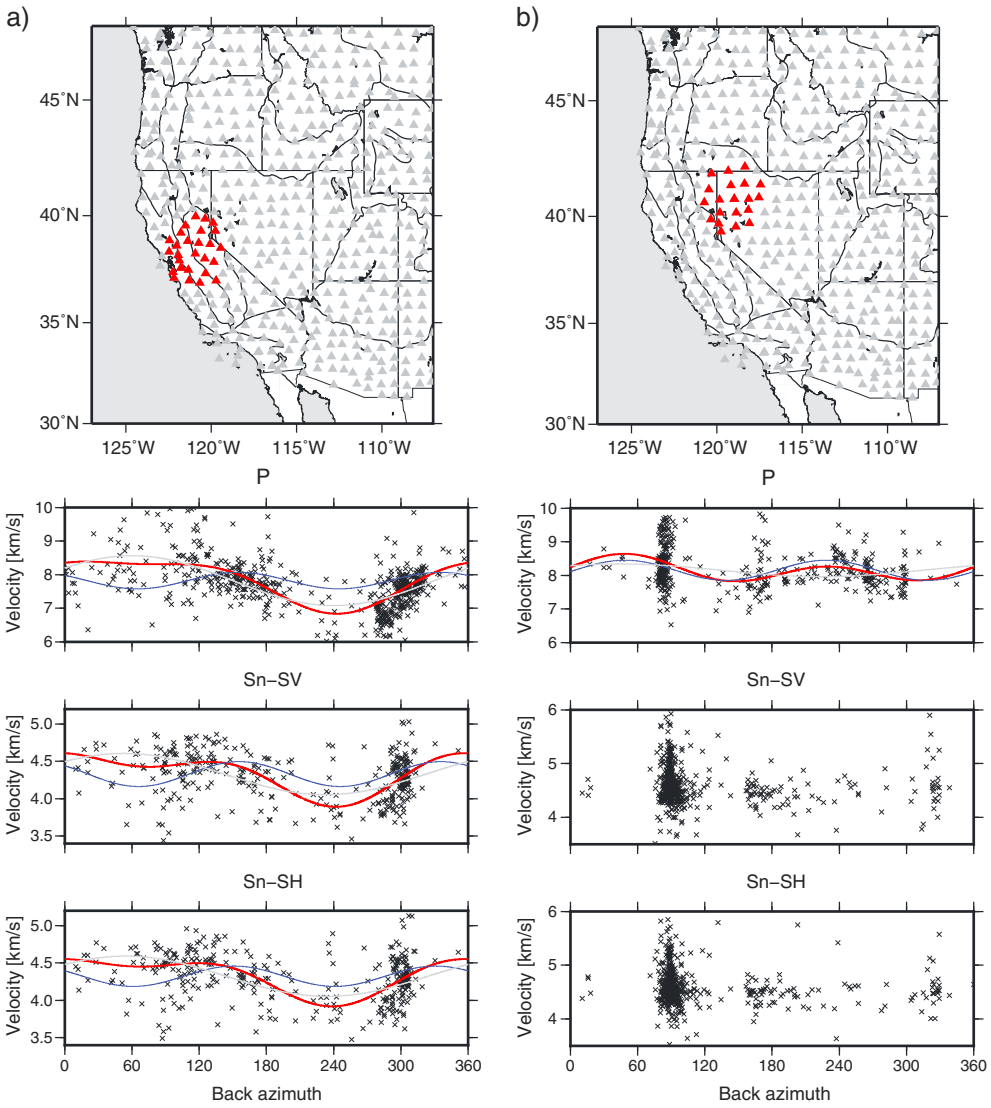

Figure 4. Azimuthal velocity variations for two regions for *P*, *Sn-SV*, and *Sn-SH* as measured at the stations indicated in red. (a) An example where we observe similar azimuthal variations for both *Sn-SH* and *Sn-SV*. (b) Velocity measurements for this subarray are scattered, indicating that the *Sn* amplitude in this region is too weak for good interstation cross correlations, and no pattern is visible. The measurements are fitted with a curve, $V\text{app} = A+[B\sin\phi+C\cos\phi]+[D\sin 2\phi+E\cos 2\phi]$, shown in red. The 1ϕ contribution that accounts for Moho dip is shown in grey, and the 2ϕ signal accounting for azimuthal anisotropy is shown in blue.

which should improve our understanding of imaged anomalies by identifying regions where properties other than temperature influence seismic velocities. Our strategy is as follows:

We first apply traditional modified time-term analysis [e.g., *Hearn*, 1996] to the *Sn* data alone to inspect the agreement between the *Sn* and *Pn* results and further assess the quality of the picks. We then continue with a joint *Pn-Sn* analysis, starting with a 1-D time-term analysis to determine the best-fitting average uppermost mantle *Pn* and *Sn* velocities and to obtain an estimate for lateral Moho depth and crustal *Vp/Vs* variations in the region. Next we perform joint inversions to solve for the lateral *Pn* and *Sn* velocity perturbations and finally add anisotropic model parameters to obtain our preferred uppermost mantle models. We assess the model resolution and trade-off between the various model parameters with a series of synthetic checkerboard tests.

2.3.1. Initial Time-Term Model

Time-term modeling has been done for many years in refraction studies to obtain average regional uppermost mantle velocity and crustal thickness estimates [e.g., *Bath*, 1978]. Traditionally, the head wave along the Moho is described with three terms, accounting for the two crustal legs of the raypath near the station

and event, and for the remaining path in the mantle. Here we apply the time-term method to obtain average *Pn* and *Sn* velocity, and an estimate for crustal thickness variations in the region. We then use the obtained residuals in the subsequent 2-D tomography to solve for lateral velocity perturbations and anisotropy. The *Pn* and *Sn* arrival times at station *s* from event *e*, t_{es}^{Pn}, and t_{es}^{Sn}, respectively, are expressed as

$$t_{es}^{Pn} = \delta_{es} S_0^P + \tau_s^p + \tau_e^p$$
$$t_{es}^{Sn} = \delta_{es} S_0^S + \tau_s^s + \tau_e^s,$$

where δ_{es} is the epicentral distance, S_0 the average slowness below the Moho, and τ_s and τ_e the station and event time terms, respectively. The time terms, which account for the time the ray spends in the crust, are a function of crustal thickness, and crustal and uppermost mantle velocities:

$$\tau_s = H \frac{\sqrt{1 - S_0^2 V_c^2}}{V_c}$$

$$\tau_e = (H - h) \frac{\sqrt{1 - S_0^2 V_c^2}}{V_c}$$

where *H* is the crustal thickness, *h* the hypocenter depth, and V_c the crustal velocity. We solve for the uppermost mantle velocities, and the station and event time terms in a least squares sense. The 1-D time term models fit the data much better than a simple straight line, especially since we are using both continental and offshore earthquakes with considerable changes in crustal thickness. The best-fitting average velocities are 7.96 km/s and 4.51 km/s for *Pn* and *Sn*, respectively. Since hypocenter depths in catalogs generally are subject to large error, only τ_s parameters are used to analyze crustal structure. Using the resulting first-order estimate of the Moho topography and the mean upper mantle velocities, we calculate the locations of the Moho piercing points for approximate ray tracing for the subsequent 2-D tomography, assuming the ray obeys Snell's law and a constant crustal velocity of 6.3 km/s, and without taking the dip of the Moho into account. Since the *Pn* time terms are better constrained than the *Sn* terms, we use the depth estimates from *Pn* alone to compute the raypath geometries for both *Pn* and *Sn*.

Linear regression to the *Pn* and *Sn* residuals can provide information on the raypath averaged change of *S* wave velocity relative to *P* wave velocity [e.g., *Schmandt and Humphreys*, 2010]. For a Poisson solid, a residual ratio of about 2.2 indicates normal thermal effects while a value near 4 suggests partial melting [e.g., *Ritzwoller et al.*, 1988]. We apply a total least squares fit to the *Pn* and *Sn* residuals obtained from the time-term analysis (Figure 5a) and obtain a slope of 3.02 with a bootstrap standard deviation of 0.07, indicating that factors other than temperature cause the velocity variations. For comparison, *Schmandt and Humphreys* [2010] found a residual ratio of 2.84 for the same region, based on teleseismic body wave residuals from upper mantle tomography.

Figure 5b displays the *Pn* and *Sn* residual density as a function of epicentral distance. The majority of the raypaths are shorter than 800 km. No systematic deviations from the 1-D time term fit are discernible apart from a slight curvature of the *Pn* residuals around 1200 km.

2.3.2. 2-D Joint *Pn-Sn* Tomography

Several approaches and algorithms to jointly invert for *P* and *S* wave velocities have been suggested [e.g., *Conder and Wiens*, 2006; *Thurber*, 1993; *Tryggvason et al.*, 2002; *Zhang and Thurber*, 2003]. The USArray data set contains fewer *Sn* picks than *Pn*, and the *Sn* picks are generally of lower quality. We therefore prefer an algorithm that couples the *Pn* and *Sn* velocity inversion. However, our database generally does not have an *Sn* pick for every corresponding *Pn* arrival and vice versa, therefore we avoid methods based on *P-S* differential arrival times in order to keep as much data as possible. We follow *Conder and Wiens* [2006] and simultaneously solve for perturbations to the average *Vp* and *Vp/Vs* without the use of differential times and describe the *Pn* and *Sn* residuals between event *e* and station *s* with the following equations:

$$\delta t_{es}^{Pn} = \Sigma \Delta_{esk} \delta s_k + \delta \tau_e^{Pn} + \delta \tau_s^{Pn}$$
$$\delta t_{es}^{Sn} = \Sigma \Delta_{esk} (\delta s_k R_0 + \gamma S_0^P \delta r_k) + \delta \tau_e^{Sn} + \delta \tau_s^{Sn},$$

where Δ_{esk} is the distance the ray travels in the cell *k*, δs_k and δr_k the slowness and *Vp/Vs* perturbation in cell *k*, and S_0 and R_0 the average uppermost mantle *P* wave slowness and *Vp/Vs* ratio. *Conder and Wiens* [2006]

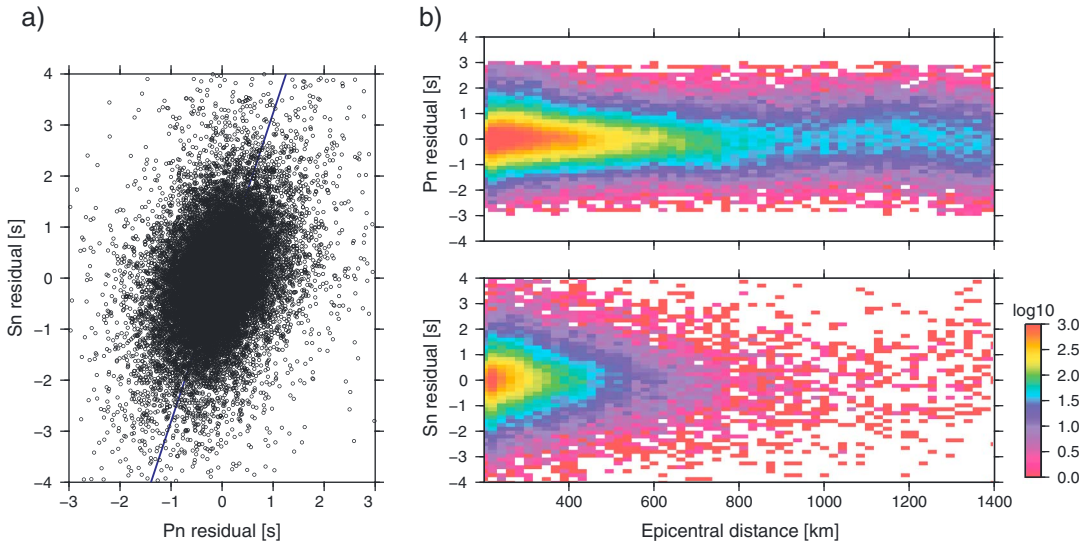

Figure 5. (a) *Pn* and *Sn* residual plot for common station and events. The line from a total least squares fit has a slope of 3.02 with a standard deviation of 0.07 from bootstrap resampling. (b) *Pn* (top) and *Sn* (bottom) residual density plot, showing the residual count in 0.1 s × 20 km intervals.

noted the importance of considering the difference in magnitude between the average slowness S_0 and *Vp*/*Vs* ratio R_0, which can cause problems in ill-posed inversions, which is typically the case in seismic tomographies with limited ray coverage. To fix this problem they suggest using a weighting parameter γ for the *Vp*/*Vs* derivatives to equalize the emphasis on the model parameters. In addition, we apply Tikhonov regularization to stabilize the resulting system $d = Gm$ by adding both smoothing and damping constraints for the δs_k and δr_k parameters and solve it in a least squares sense with a conjugate gradient solver. We run inversions for several different regularization parameters to obtain trade-off curves and various models with both synthetic and real data.

Anisotropy can significantly influence the observed seismic velocities, and if not accounted for it could translate to wrongly mapped structures, especially in regions with a dominant raypath direction. We follow *Hearn* [1996] and add anisotropic parameters to the *Pn* equation according to the derivations by *Backus* [1965], described above, for a modified time term inversion:

$$\delta t_{\mathrm{es}}^{Pn} = \Sigma\Delta_{\mathrm{esk}}(\delta s_k + B1_k \cos 2\phi_{\mathrm{esk}} + B2_k \sin 2\phi_{\mathrm{esk}}) + \delta\tau_e^{Pn} + \delta\tau_s^{Pn}$$

$$\delta t_{\mathrm{es}}^{Sn} = \Sigma\Delta_{\mathrm{esk}}(\delta s_k R_0 + \gamma S_0^P \delta r_k) + \delta\tau_e^{Sn} + \delta\tau_s^{Sn}$$

where ϕ_{esk} is the back azimuth in cell k. As in *Pn*-only tomography [*Buehler and Shearer*, 2010], we neglect any possible 4ϕ *Pn* azimuthal variations because previous studies of mantle anisotropy have generally found the 2ϕ terms to dominate [e.g., *Raitt et al.*, 1969; *Christensen*, 1984]. For completeness we prefer to add anisotropic parameters to the *Sn* picks as well, assuming they measure *SV* energy, which seems reasonable since we did not find any evidence for 4ϕ velocity variations:

$$\delta t_{\mathrm{es}}^{Pn} = \Sigma\Delta_{\mathrm{esk}}(\delta s_k + B1_k \cos 2\phi_{\mathrm{esk}} + B2_k \sin 2\phi_{\mathrm{esk}}) + \delta\tau_e^{Pn} + \delta\tau_s^{Pn}$$

$$\delta t_{\mathrm{es}}^{Sn} = \Sigma\Delta_{\mathrm{esk}}(\delta s_k R_0 + \gamma S_0^P \delta r_k + E1_k \cos 2\phi_{\mathrm{esk}} + E2_k \sin 2\phi_{\mathrm{esk}}) + \delta\tau_e^{Sn} + \delta\tau_s^{Sn}$$

Diaz et al. [2013] reported increased continuity and sharpness for their imaged *Sn* perturbations with the inclusion of anisotropic parameters but also caution against strong interpretation of the *Sn* results. We believe the inclusion of anisotropic parameters to describe *Sn* makes sense, since we found azimuthal velocity dependence for localized regions. In addition, it seems unlikely that a physical model would only cause an azimuthal dependence for *Pn* waves but not *Sn* waves. Assuming hexagonal symmetry with a horizontal symmetry axis, the *P* and *SV* wave anisotropy is coupled as the wave travels fastest in the same direction. Since uppermost mantle anisotropy is typically well modeled with hexagonal symmetry, we require the

Pn and *Sn* fast axis to point in the same direction in our tomography. To satisfy this constraint, the ratio of the $B1/B2$ and $E1/E2$ parameters need to be equal in each cell: $E1_k = \kappa B1_k$ and $E2_k = \kappa B2_k$:

$$\delta t_{es}^{Pn} = \Sigma\Delta_{esk}(\delta s_k + B1_k \cos 2\phi_{esk} + B2_k \sin 2\phi_{esk}) + \delta\tau_e^{Pn} + \delta\tau_s^{Pn}$$

$$\delta t_{es}^{Sn} = \Sigma\Delta_{esk}(\delta s_k R_0 + \gamma S_0^P \delta r_k + \kappa B1_k \cos 2\phi_{esk} + \kappa B2_k \sin 2\phi_{esk}) + \delta\tau_e^{Sn} + \delta\tau_s^{Sn}$$

Unfortunately, this constraint makes the system more complex, since we neither know κ nor the anisotropic parameters $B1$ or $B2$. To simplify the problem, it seems reasonable to assume that κ is constant for all the cells to avoid adding too many model parameters. For equal *P* and *S* anisotropy in percent, defined as $[V_{max} - V_{min}]/V_{average}$), κ corresponds to the velocity ratio *R*. Note that κ equals zero for no azimuthal shear velocity variations. Observations and laboratory experiments provide guidance for reasonable κ values. Generally, it is not simple to determine the relationship between the amount of *P* and *S* anisotropy in rocks [*Levin and Park*, 1998], but *P* anisotropy is generally observed to be stronger than *S* anisotropy in the upper mantle, although estimates span a fairly large range [e.g., *Ismail and Mainprice*, 1998; *Babuska and Cara*, 1991]. *Keith and Crampin* [1977] provide elastic tensor components for uppermost mantle material with 6.59% azimuthal anisotropy for horizontally propagating *SV* polarized waves, and 13% for *P* waves. Determining the optimal κ value based on data misfit criteria is complicated by the regularization we apply in our inversions. Checkerboard tests (see below) for inversions with damping show that recovered anisotropy amplitudes are generally underestimated, and this would artificially increase the value of κ. Omitting any damping constraints but keeping Laplacian smoothing, we find the data misfit to be smallest for a *Pn* to *Sn* anisotropy ratio of ~1.4.

2.4. Data Coverage and Resolution Tests

Azimuthal coverage is key in analyzing anisotropy because only in azimuthally well sampled regions can anisotropy be distinguished from isotropic anomalies. Figure 6 shows the azimuthal ray coverage with pie wedges for both *Pn* and *Sn* in 2 by 2° cells (this is larger than the 0.25° cells used in tomography but gives enough space for plotting). Azimuthal coverage is good in the westernmost states and the Basin and Range Province. The color scale in Figure 6 indicates the ray count. *Pn* rays sample the model region well except for small areas at the edge of the model. *Sn* ray coverage is lower east of longitude 110°W, probably partly because the catalog is not complete and also because of fewer natural sources in this region.

Tests with synthetic data are useful to show which parts of the model structure are resolvable for big problems where it is difficult to compute the generalized inverse. This assumes that the simplified model parametrization adequately describes the real wave propagation. Figure 7 shows the output of two checkerboard tests with sinusoidal velocity perturbations with a half wavelength of 2° for *Sn* raypaths only. Figure 7a is output from synthetic data generated with isotropic perturbations only. We used the same station and event distribution as for the real observations and let the velocity vary between ±5%. We added normally distributed noise with a standard deviation of 0.9 s to the synthetic picks (the median analyst-assigned error to the *Sn* picks in the USArray database is 0.87 s). The isotropic structure is generally well recovered, but there is considerable anisotropic leakage where velocity changes are large. In Figure 7b the input contains both isotropic and anisotropic perturbations of ±5%, with north-south east-west alternating fast axes in adjacent tiles. These *Sn* tomography maps from synthetic data show that ray coverage should be good enough, assuming mostly *SV* energy, to resolve azimuthal velocity dependence in California and Nevada.

Next we show two synthetic tests for the joint *Pn-Sn* inversion. For Figure 8 (top), we generate data with 5% *Pn* anisotropy, and ±3% *Vp* and *Vp/Vs* perturbations in adjacent 2° cells. We add random noise with 0.5 s standard deviation. For the second example we only use ±3% isotropic *Pn* velocity perturbations, to assess the amount of leakage into the other parameters (this will generally depend on the choice of regularization parameters). *Pn* azimuthal ray coverage is not ideal everywhere, but good enough to resolve the *Pn* fast directions for a large region. The anisotropy amplitudes are less well recovered outside the Basin and Range Province and California. It seems unavoidable to have leakage between the model parameters for reasonable regularization. For purely isotropic input, there is leakage into both the anisotropic and *Vp/Vs* parameters. Anisotropic leakage is again largest at the nodes of slow and fast isotropic perturbations, indicating that isotropic anomalies might introduce artificial anisotropy at their edges.

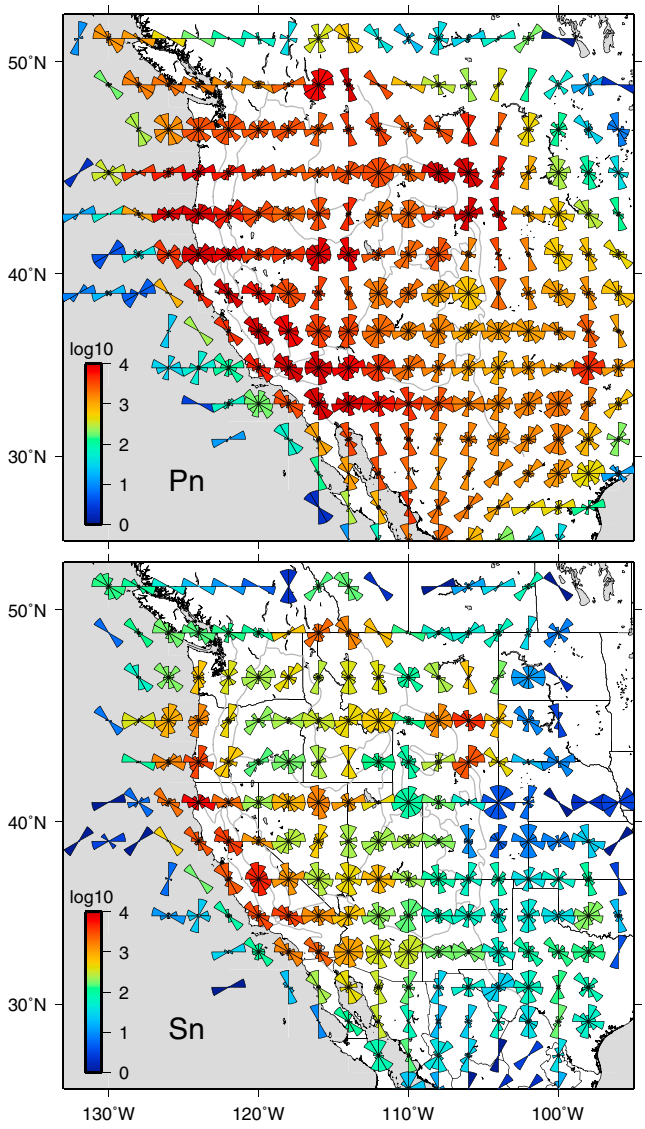

Figure 6. Azimuthal coverage for (top) *Pn* and (bottom) *Sn* displayed with pie wedges. The color scale shows the ray count.

3. Results and Discussion

3.1. Separate *Sn* Tomography

We preformed separate *Sn* tomography mainly to test the viability of the *Sn* picks. Not including small-scale active source studies, the only other attempt on *Sn* tomography in the western United States to our knowledge was conducted by *Nolet et al.* [1998]. However, the study was pre-USArray, using only about 3500 *Sn* picks, which limited the model resolution. Our isotropic *Sn* velocities are plotted in Figure 9a, together with the results from separate *Pn* tomography for comparison in Figure 9b. Generally, the large-scale *Sn* anomalies are in good agreement with the ones from a purely *Pn* inversion. This shows that the *Sn* picks contain useful signal despite their greater scatter.

The largest differences between our *Pn* and *Sn* tomography maps are the larger *Sn* low-velocity anomalies seen beneath the Colorado Plateau and central Wyoming. The shear velocity map at Moho + 4 km (upper mantle) depth from the ambient noise data of *Bensen et al.* [2009] shows a similar strong low-velocity zone for much of Utah and northern Arizona, without any corresponding low-velocity anomalies at Moho − 4 km (lower crust) depth or at 80 km depth for this region. *Steck et al.* [2011] also measure higher-than-average crustal Sg velocities for the Colorado Plateau. It appears that the jump in shear velocity across the Moho below the Colorado Plateau is relatively small.

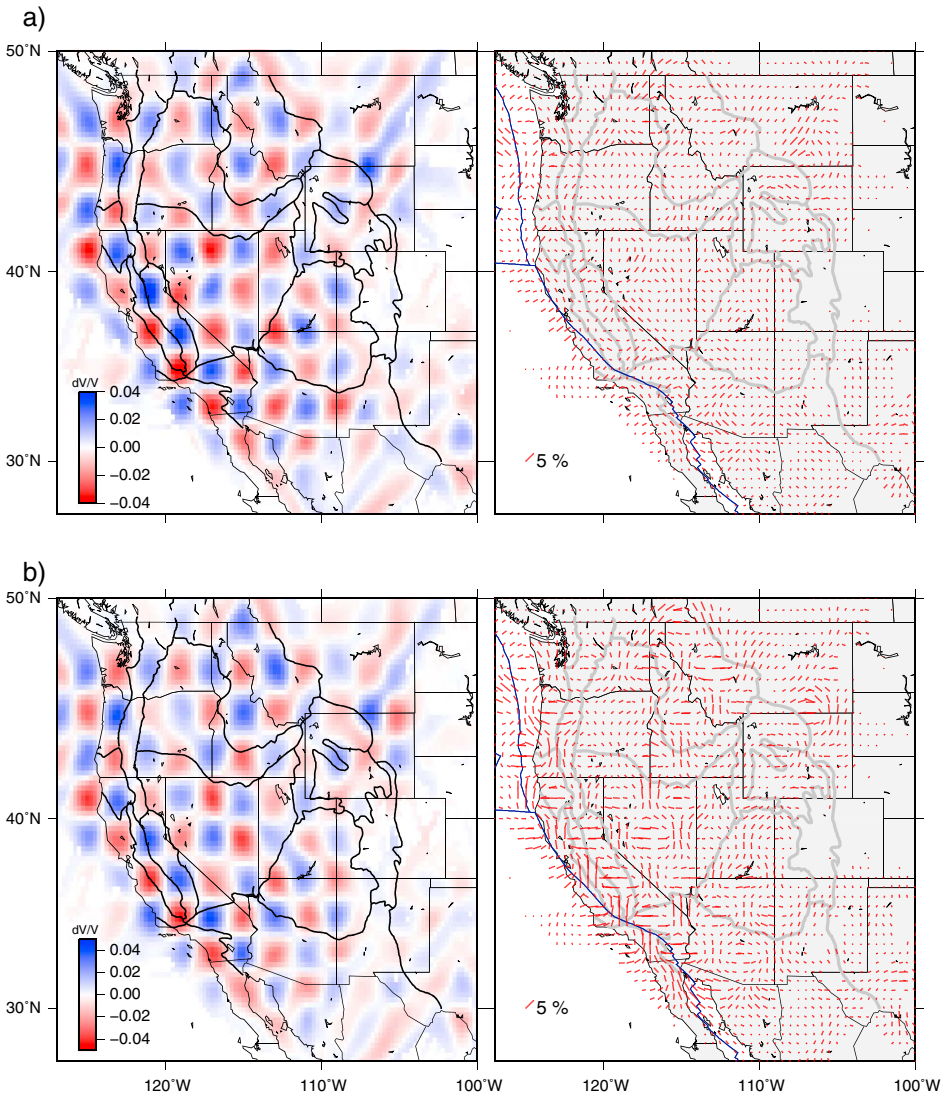

Figure 7. Synthetic checkerboard test with *Sn* data only. (a) The recovered models from a test with ±5% isotropic perturbations only. (b) Recovered maps from a test that includes both isotropic and anisotropic perturbations.

Although looking at the fast directions obtained from *Sn* tomography alone (Figure 9c) can help to understand the nature and quality of the *Sn* picks, interpretations should be made with caution. *Diaz et al.* [2013] performed *Sn* tomography for the Euro-Mediterranean region and found sharper velocity perturbations with better lateral continuity when anisotropic terms are included in the inversions. Similarly, we find that adding anisotropic parameters to the *Sn* inversion produces more focused isotropic anomalies. However, for reasons that we do not completely understand, the *Pn* and *Sn* fast directions generally do not agree (compare Figure 9c with 9d).

3.2. Joint Tomography Results

3.2.1. *Vp* and *Vp*/*Vs* Structure

The images in Figure 10 show the isotropic *Pn* velocities and *Vp*/*Vs* ratio for the three different inversion schemes. The inclusion of anisotropic parameters for *Sn* does not significantly lower the data variance (Table 1). Judging by the tomographic maps and data fit, there is either no significant shear anisotropy for most regions below the western United States, or the error of the shear wave picks is too large to resolve the relatively small anisotropic signal, or the assumption of hexagonal symmetry with a horizontal symmetry axis is not valid. Since *Pn* and surface wave tomographies show a heterogeneous but similar anisotropic structure below the western United States, it is likely that there is too much scatter in the *Sn* picks to detect

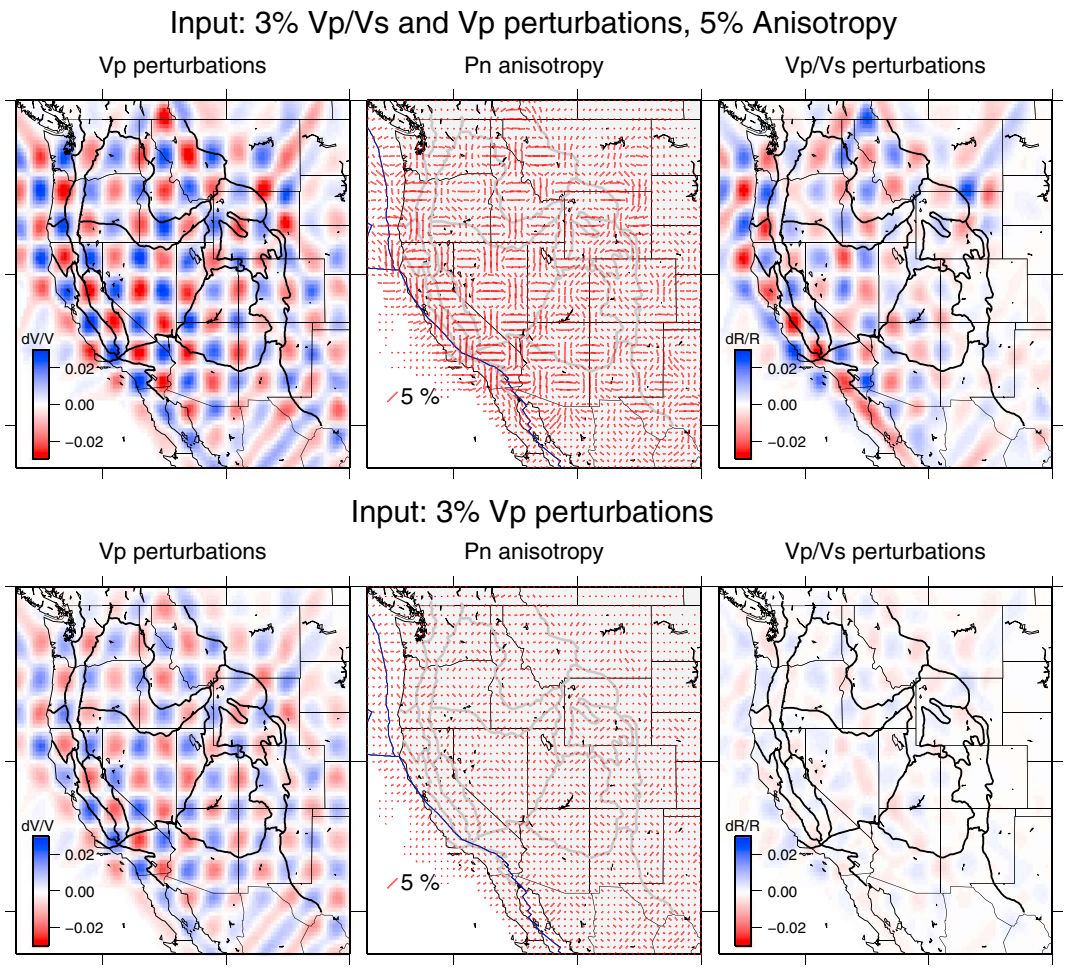

Figure 8. Checkerboard tests for the joint inversion. (top) Recovered models from synthetic data with 5% *Pn* anisotropy, and ±3% *Vp* and *Vp*/*Vs* perturbations in adjacent 2^o cells. Random noise with 0.5 s standard deviation was added. (bottom) We used only ±3% isotropic *P* velocity perturbations, to assess the amount of leakage into the other parameters.

anisotropy. Nevertheless, the inclusion of both *Pn* and *Sn* anisotropy, with consistent fast directions, makes the model more physically realistic. This is our preferred model because it results from an inversion approach that is most consistent with anisotropic observations and aligned olivine models.

Model parameter uncertainty due to picking errors alone can be estimated with a Monte Carlo technique [*Houser et al.*, 2008], where the inversion process is repeated many times with Gaussian distributed noise added to the data. The parameter errors are uniform over most of the region and do not exceed 0.02 km/s for the *Pn* velocities and 0.005 for the velocity ratio. These values are lower bounds on the error estimates as uncertainties from other contributions, such as the choice of model parameterization and regularization, are not considered.

One of the most prominent low-velocity anomalies in the uppermost mantle beneath the western United States is located below the Snake River Plain. This anomaly appears to range vertically from the Moho to about ~200 km depth [*Schmandt and Humphreys*, 2010; *Tian and Zhao*, 2012]. The *Vp*/*Vs* in this region is high (~1.8). These observations are in agreement with a partially molten upper mantle below the Yellowstone hot spot track because the existence of partial melt or fluids in the uppermost mantle should affect the shear wave velocity more drastically than the compressional velocity [e.g., *Takei*, 2002].

The other two large high *Vp*/*Vs* anomalies are situated in central Wyoming and below the bulk of the Colorado Plateau. Since the raypaths that cover Wyoming are mostly from low-magnitude quarry blasts, we will not focus on this structure. The high *Vp*/*Vs* anomaly below the Colorado Plateau is interesting as it is in contrast with *Pn* and other body wave velocities measured in this region, which are typically lower in

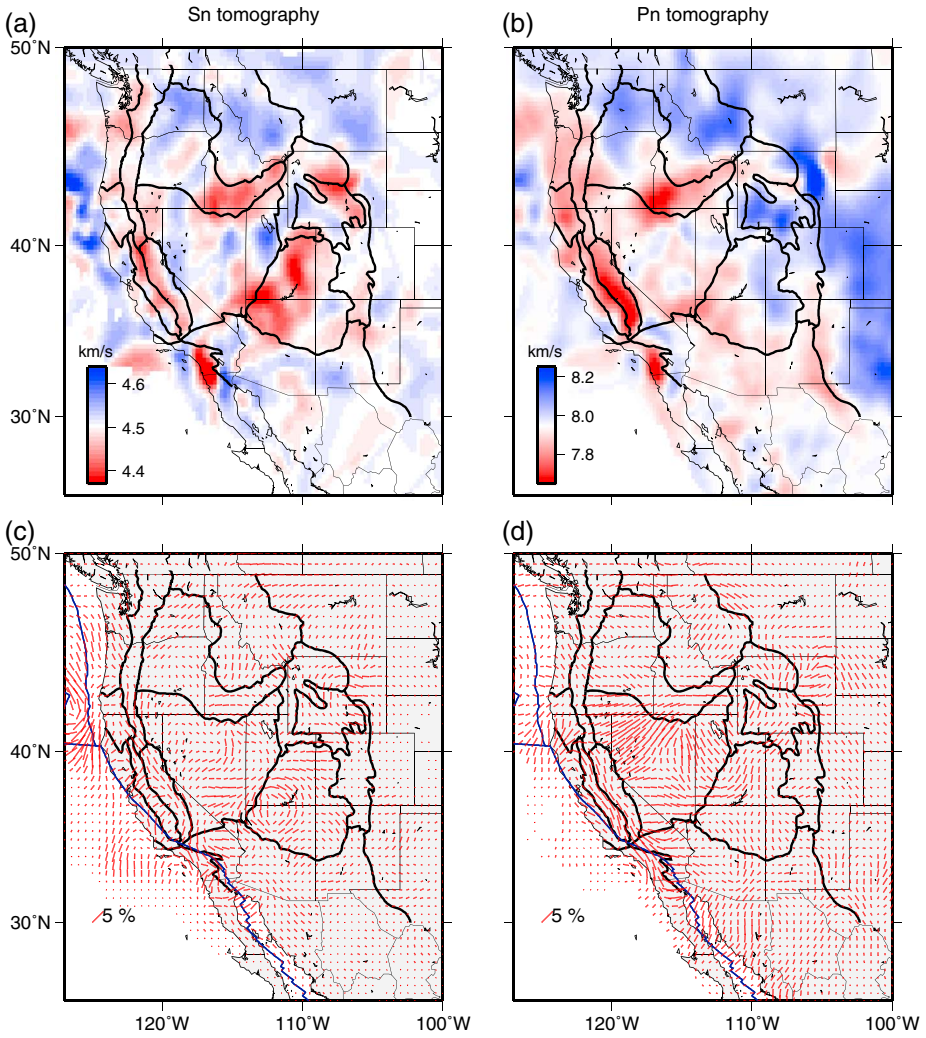

Figure 9. Comparison of tomography results for separate anisotropic (a and c) *Sn* and (b and d) *Pn* inversions. Figure 9a shows the retrieved isotropic *Sn* velocities and Figure 9c the corresponding fast directions. Figures 9b and 9d show the equivalent maps for *Pn*.

the southwest and higher in the northeast [*Obrebski et al.*, 2011; *Schmandt and Humphreys*, 2010]. Comparison of our uppermost mantle *Vp*/*Vs* map to the images at 90 km depth by *Schmandt and Humphreys* [2010], which show average to high *P* and *S* velocities for most of the Colorado Plateau, suggests significant changes in shear velocity structure in the top 50 km of the mantle. *Levander et al.* [2011] presented an additional *Vp*/*Vs* map at 80 km depth beneath the Colorado Plateau from a similar body wave tomography study as in *Schmandt and Humphreys* [2010], which shows low shear wave velocities and high *Vp*/*Vs* beneath the periphery of the plateau surrounding a higher-velocity core. They interpret this seismically imaged core as a lithospheric drip, which delaminates from the base of the lower crust of the Colorado Plateau. If the lithospheric drip has detached completely from the base, and asthenospheric material has taken the space of the removed lithosphere, it would make sense to observe a different seismic structure in the top kilometers of the mantle with generally high *Vp*/*Vs*. This argument, however, is in contrast with the relatively high *Pn* velocities in the northeastern section below the Colorado Plateau, unless we assume that the lithosphere below this northeasternmost region is intact (in agreement with the sketch by *Levander et al.* [2011]) and that the shear anomaly is somewhat smeared out because of lower ray coverage further east.

Regions with low *Vp*/*Vs* anomalies typically are more complicated to explain. Figure 10 shows very low *Pn* velocities and low *Vp*/*Vs* below the Sierra Nevada for all the models, but the anomaly appears more pronounced if we account for anisotropy. This low *P* velocity anomaly is consistent with the older *Pn* study by *Hearn* [1996] but appears to be confined to the very top of the mantle below the Sierra Nevada,

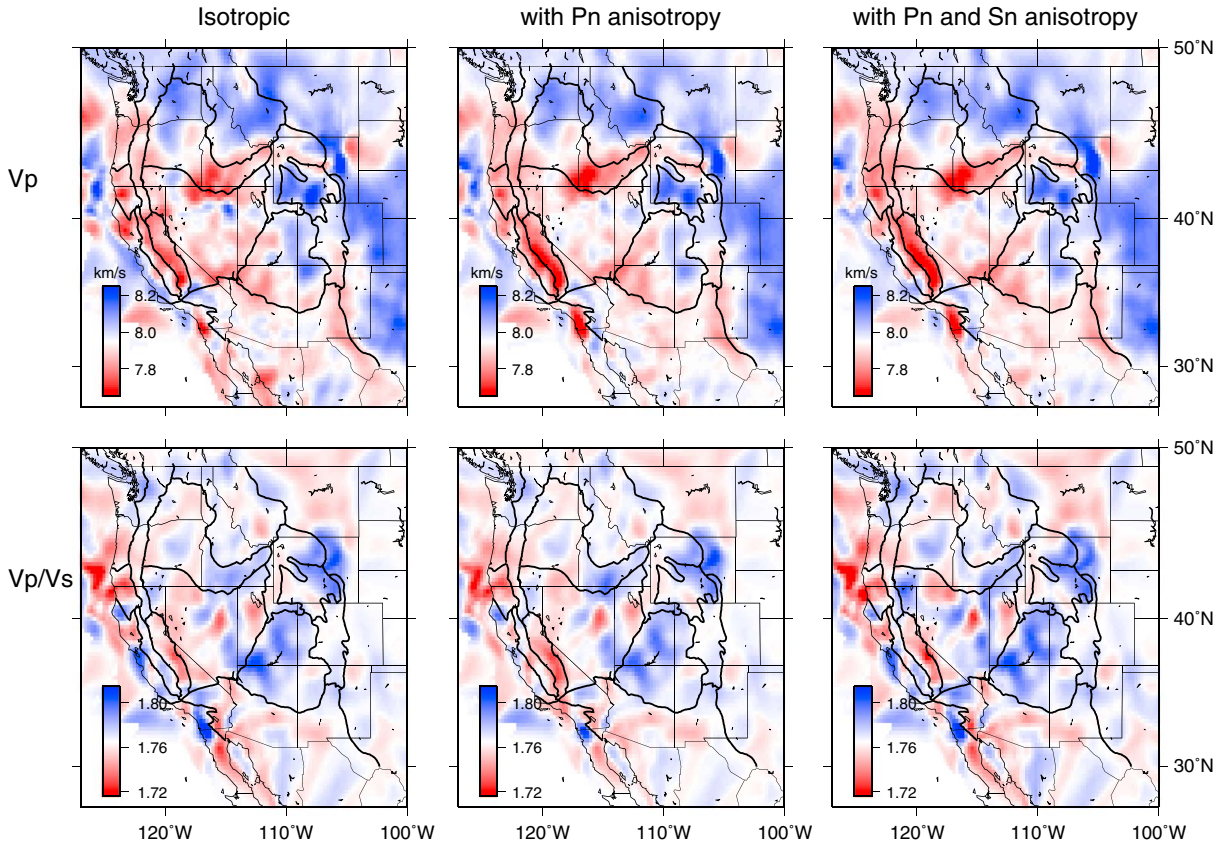

Figure 10. *Vp* and *Vp/Vs* from joint *Pn-Sn* tomography. (left) Contains no anisotropic parameters. (middle) *Pn* anisotropy is added. (right) Contains both *Pn* and *Sn* anisotropy of equal magnitude.

and tomography slices from *Schmandt and Humphreys* [2010] and *Tian and Zhao* [2012] at 90 km and 65 km depth, respectively, show high-velocity anomalies associated with the Juan de Fuca slab in this region. *Jones et al.* [1994] suggested that the uppermost mantle below the Sierra Nevada is unusually warm. Studies of xenoliths indicate that mantle lid beneath the Sierra Nevada has been removed since cicra 10 Ma, and seismic analysis suggests that the removed material is descending deeper into the mantle west of the range [e.g., *Saleeby and Foster*, 2004]. Upwelling of hot asthenospheric material would explain the very low uppermost mantle *Pn* velocities. However, the *Sn* anomaly is much less strong, and the observation of low *Vp/Vs* is puzzling as higher values would generally be expected in such a regime. A change in composition, such as enrichment in orthopyroxene in the upper mantle [*Soustelle and Tommasi*, 2010] or the presence of pore fluids [*Takei*, 2002] could lead to locally lower *Vp/Vs*. Since the Farallon Plate subduction beneath the western

Table 1. Root-Mean-Square Errors for the Various Models

	RMSE (*s*)	
Fitting method	*Pn*	*Sn*
Straight line fit	1.49	2.46
1-D time term	0.67	0.91
2-D isotropic stand-alone *Sn*		0.84
2-D anisotropic stand-alone *Sn*		0.81
2-D anisotropic stand-alone *Pn*	0.57	
2-D isotropic joint	0.60	0.84
2-D joint, with *Pn* anisotropy only	0.57	0.84
2-D joint, with equal *Pn* and *Sn* anisotropy	0.57	0.82
2-D joint, with *Pn/Sn* anisotropy = 2	0.57	0.83
Mean (median) analyst-assigned picking error (s)	0.54 (0.42)	1.10 (0.87)

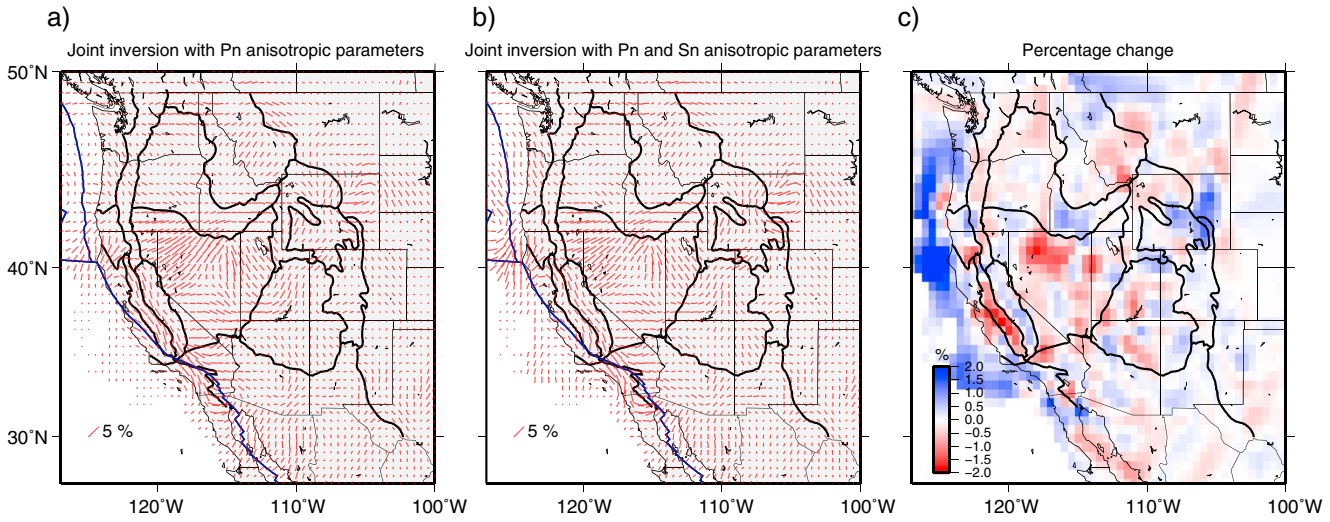

Figure 11. Fast axis obtained from (a) an inversion that only accounts for *Pn* anisotropy and (b) from an inversion that includes *Sn* anisotropy with equal strength. (c) The change in percentage between Figures 11a and 11b.

United States is believed to have experienced a period of flat subduction during the Laramide orogeny, it is interesting to note that these characteristics—low *P* velocity and low *Vp*/*Vs*—are similar to the recent observations by *Wagner et al.* [2006] for the upper mantle above the flat slab subduction in Chile and Argentina but differ from seismic properties of subduction zones with steeper slabs.

3.2.2. Anisotropy

Figure 11a shows the fast direction we obtain from a *Pn*-*Sn* joint inversion that only allows the *Pn* velocity to vary with azimuth. These *Pn* anisotropic modeling results generally show a quite complex image but do not deviate much from our previous results with *Pn* data alone that are discussed in [*Buehler and Shearer*, 2010]. The main anisotropic features include the SW-NE fast axis in northwestern Nevada, east-west anisotropy off the coast of northern California and Oregon, and mostly fault-parallel fast axes in Central California. The fault-parallel fast axis indicates that the anisotropy in this region is caused by shearing along the plate boundary, but similar to *Hearn* [1996], we find that the fast axis is not parallel to the plate boundary in all of southern California but is east-west in the Mojave Desert. *Hearn* [1996] suggests north-south compression in southern California for the possible cause of the perpendicular east-west anisotropic direction. The strong anisotropy off coastal Oregon could be correlated with the subduction zone. However, large isotropic anomalies can also be observed in this area, which could indicate a modeling artifact since azimuthal coverage in these cells is limited.

For completeness we include *Sn* anisotropic parameters, as it would not be realistic to allow for an azimuthal dependence for *Pn* only. This is somewhat problematic, as the *Sn* picks appear not to be good enough to resolve anisotropy and the fast axis directions from separate *Pn*, and *Sn* tomographies are largely uncorrelated. However, the inclusion of *Sn* anisotropic parameters has overall only minor effects, and the fast directions are mostly constrained by the larger number of *Pn* data for *P* to *S* anisotropy ratios larger than 1. In Figure 11b we display the fast directions as obtained from an inversion that includes *Sn* anisotropy, with a prescribed *Pn* to *Sn* anisotropy ratio of 1, which is probably larger than expected, but serves as an end-member for comparison to fast directions from *Pn* data only. Most notably, the inclusion of *Sn* requires stronger anisotropy off the western coast. Azimuthal coverage in this region, however, is bad, and *Sn* tomography shows patches of strong isotropic anomalies that typically are associated with an increase in leakage between model parameters as indicated by the checkerboard tests.

3.2.3. Crustal Thickness and *Vp*/*Vs* Structure

The major part of the signal in the station time terms can be explained with changes in crustal thickness, and a first-order estimate of the Moho depth of the region is easily obtained by assuming a constant crustal velocity. Each thickness measurement represents an average over a cone defined by the ray incident angles and Moho depth. Event time terms are generally not used as they are subject to large error because of often poorly constrained hypocenter depths. The assumption of constant crustal velocity, however, does not appear very realistic, and recent research confirms that the crustal velocity in the western United States is

very heterogeneous, both laterally and vertically [e.g., *Moschetti et al.*, 2010b; *Steck et al.*, 2011]. With both *Pn* and *Sn* time terms it is possible to gain insight into both crustal thickness and vertically averaged crustal velocities [e.g., *Haines*, 1980], although they cannot be interpreted unambiguously without any independent constraints. However, the relationship between crustal thickness and the crustal *P* or *S* velocity is close to linear, and the crustal *Vp*/*Vs* relatively insensitive to small changes in thickness.

Since the *Pn* and *Sn* station time terms have zero mean (set as a constraint in the inversion process because of the trade-off between the station and event terms), we first estimate the time contribution from the average crustal thickness and velocity structure in the region in order to obtain absolute times. We accomplish this by fitting a straight line to time-distance points of shallow continental earthquakes to measure the intercept time for both *Pn* and *Sn* data. We then add half of that intercept time to the relative station time terms. The intercept times suggest average crustal *P* and *S* velocities of 6.07 km/s and 3.48 km/s for an average crustal thickness of 35 km, and 6.39 km/s and 3.68 km/s for a 40 km crust, respectively. Values between these two estimates seem most likely. For comparison, *Chulick and Mooney* [2002] found an average crustal thickness for the North American continent of 36.72 km with average *P* and *S* velocities of 6.29 km/s and 3.65 km/s. Recent USArray receiver function studies [*Gilbert*, 2012; *Levander et al.*, 2011; *Lowry and Perez–Gussinye*, 2011] seem to show average crustal thickness values between ~38 and 40 km. We proceed with assuming an average crustal thickness of 38.5 km with corresponding mean crustal *P* and *S* velocities of 6.30 km/s and 3.61 km/s, respectively.

Next we calculate crustal thickness separately as inferred from the *Pn* and *Sn* time terms, assuming these homogeneous crustal velocities. Figure 12a shows the crustal thickness estimates below each receiver (after correcting for station elevations). These Moho depth estimates show a relatively smooth image even though no regularization is applied to the time terms in the tomography. The crust gradually thickens from the southern Basin and Range across the Colorado Plateau to a maximum below the Wyoming Basin and the southern Rocky Mountains. The map also shows thin crust for the central Basin and Range compared to deeper Moho depths below the western mountain ranges. Crustal *P* velocity in the western United States is not constant, however, and introduces errors in regions of crustal velocity anomalies. In Figure 12b we show the crustal thicknesses inferred from *Pn* time terms using the laterally varying vertically averaged crustal velocities compiled by *Chulick and Mooney* [2002]. The lower-than-average velocities for most of the western and southern margin reduces the crustal thickness estimates for these regions. On the other hand, the higher crustal velocities below the Great Plains increase the corresponding Moho depths. Note that the low values at the northeastern model boundary are associated with larger errors and do not provide an reliable picture of crustal thickness for this region.

Figure 12c shows the inferred crustal thickness with a constant crustal *S* velocity of 3.61 km/s. The *Sn* time terms show larger scatter but overall exhibit similar features to the *Pn* station terms. It is not expected that the *Pn* and *Sn* maps agree in detail, as it is likely that the *Vp*/*Vs* ratio in the crust is not constant. Thus, differences in the *Pn* and *Sn* thickness maps indicate lateral *Vp*/*Vs* variations. It is also important to remember that the *Sn* terms are generally associated with larger errors, especially east of longitude 110°W, and that the time terms average over azimuth. These factors account for some of the observed differences, especially at stations in the east with few *Sn* arrivals.

Figure 12d shows the crustal *Vp*/*Vs* at each station location as inferred from the *Pn* and *Sn* time terms, adjusted to absolute times as described above, and using the crustal thickness displayed in Figure 12b. The ratio spans a fairly large range from ~1.55 to ~2.15 with 94% of the model points falling between 1.6 and 1.9. The variations of the *Pn* and *Sn* terms indicate higher crustal velocity ratios in the southern Basin and Range Province and Southern California. Other regions of high *Vp*/*Vs* include the crust of the Columbia Plateau, and much of the Great Basin, especially the section south of the Snake River Plain and west of the Colorado Plateau. We generally observe low values east of the Basin and Range, prominently in the southwest and northeast of the Colorado Plateau. The easternmost tip of the Snake River Plain is associated with low *Vp*/*Vs*, but the ratio is generally higher for the central portion.

Crustal thickness estimates from receiver function analysis are based on the difference in arrival times between the direct and converted wave at the crust-mantle boundary and are used to infer both crustal thickness and *Vp*/*Vs*. They generally suffer from a velocity thickness trade-off as well, and comparisons between models can provide additional insight on the most likely Moho depth. *Gilbert* [2012], *Levander et al.* [2011], and *Lowry and Perez-Gussinye* [2011] present crustal thickness estimates from receiver functions

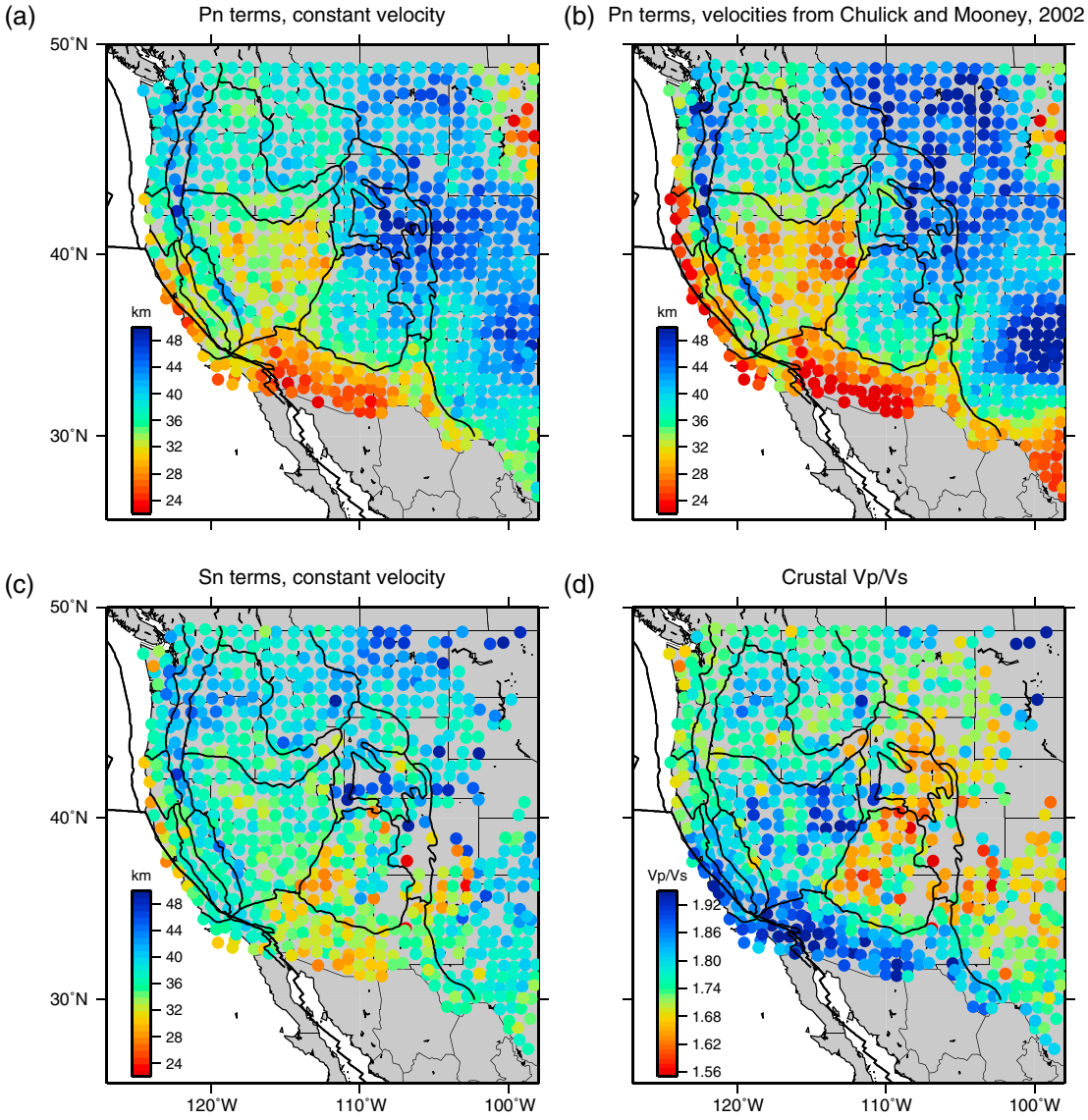

Figure 12. Crustal thickness and *Vp/Vs* estimates from *Pn* and *Sn* station time terms. (a) Crustal thickness estimates from *Pn* station terms with the assumption of a constant crustal velocity. (b) Same as Figure 12a but with lateral varying crustal *P* velocities from *Chulick and Mooney* [2002]. (c) Crustal thickness estimates from *Sn* terms with a constant crustal *S* velocity. (d) Vertically averaged crustal *Vp/Vs* from *Pn* and *Sn* time terms.

at USArray stations with different methods and a priori assumptions. Overall, the crustal thickness estimates from receiver functions and *Pn* station terms look similar, but there are discrepancies in some regions.

Generally, our crustal thickness estimates from the *Pn* time terms are larger than receiver function results along the western margin. This is especially so if we assume a constant crustal velocity in the time-term analysis and leads to thickness estimates that are about 10 km thicker than the ones measured using receiver functions by *Gilbert* [2012] below many stations along the coast of California, southern Oregon, and Washington. Using lower crustal velocities in this region, as compiled by *Chulick and Mooney* [2002], produces thinner crust, which largely agrees with the receiver function thickness estimates of *Lowry and Perez-Gussinye* [2011] along the coast of California and Oregon, but which remain somewhat thicker than those of *Gilbert* [2012]. The thicker crust required to explain the station time terms along the coast of Washington could be a result of complications with the plate boundary since many *Pn* raypaths are incident from offshore.

For the Basin and Range and Snake River Plain provinces the receiver function and *Pn* crustal thicknesses are mostly consistent and show a northward increase in Moho depth. Our thickness below the Snake River Plain

ranges from about 32 to 40 km, roughly similar to the values obtained by *Lowry and Perez-Gussinye* [2011]. *Levander et al.* [2011] show a crust about 40 km thick below the Snake River Plain from *Ps* receiver functions, but only about 35 km thick from *Sp* receiver functions. The study by *Gilbert* [2012] shows the thickest Snake River Plain crust with Moho depths exceeding 40 km. These higher values for the crustal thickness of the Snake River Plain could result from the assumption of constant *Vp*/*Vs*, as the Snake River Plain generally seems to be associated with a higher-than-average ratio, as indicated by *Lowry and Perez-Gussinye* [2011] and, less significantly, by our *Vp*/*Vs* map.

All of the above mentioned studies agree that the Moho below the southern Basin and Range is thin, bordered by the thicker crust of the Colorado Plateau and the Great Plains. However, resolving details of the crustal thickness of the Colorado Plateau has proven as problematic as the velocity structure of the upper mantle, as the Moho depth estimates are generally inconsistent between studies, even though the crust generally appears undeformed and tomographic images show mostly laterally constant crustal velocities throughout the Plateau [e.g., *Moschetti et al.*, 2010b; *Steck et al.*, 2011]. *Gilbert* [2012] discussed the difficulty of obtaining accurate receiver function measurements below the Colorado Plateau because of the presence of high-velocity layers in the lower crust, which decrease the velocity contrast across the Moho. The various crustal thickness studies show some of the biggest differences in this province: *Lowry and Perez–Gussinye* [2011] found consistently thick crust throughout the Plateau exceeding 40 km except for small patches of slightly thinner crust in the center. The Colorado Plateau crust seen by *Gilbert* [2012] generally exceeds ~42 km but shows greater variability, with very thick crust around 50 km in the southwest and along the northeastern border. We also observe an increase in thickness in the southwestern part of the Plateau, the absolute values, however, are ~10 km lower than the estimates by *Gilbert* [2012]. *Levander et al.* [2011] found a thickness of ~50 km in the north and east of the plateau thinning to about 35 km at the southern and western boundary. Our Moho depth generally increases toward the northeast as well but is shallower overall.

Our *Vp*/*Vs* estimates are generally lower for the Colorado Plateau than the values of *Lowry and Perez-Gussinye* [2011], but the overall structure with lower values at the margin and higher *Vp*/*Vs* in the center is similar. Crustal *Vp*/*Vs* estimates are often subject to relatively large errors. Differences in *Pn* and *Sn* raypaths, crustal anisotropy, and azimuthal averaging, for example, could contribute to errors in *Vp*/*Vs* estimates. Waves used for receiver function analysis have almost vertical incidence and therefore optimal lateral resolution. However, they often poorly constrain the *Vp*/*Vs* ratio; *Lowry and Perez-Gussinye* [2011] include constraints from gravity to reduce uncertainty. It is therefore not surprising that the *Vp*/*Vs* map shows some scatter and that there are differences between receiver function and time-term estimates. Consistencies include high *Vp*/*Vs* in the crust of the Columbia Plateau, Snake River Plain, the center of the Colorado Plateau, and the southern Basin and Range, as well as low *Vp*/*Vs* near the eastern Sierra Nevada, the margins of the Colorado Plateau, and the crust of the Rocky Mountains. In the northern Basin and Range, we obtain low crustal *Vp*/*Vs* for a relatively narrow region in central Nevada, surrounded in the east and west by high ratios. This structure is very different from the *Vp*/*Vs* values estimates by *Lowry and Perez-Gussinye* [2011] whose map shows low values in central and eastern Nevada. It is not yet clear what causes these differences, as the crustal thickness in this region appears to be well constrained, and no strong velocity anomaly in the uppermost mantle can be observed. Combined analysis of crustal refraction data, as explored with USArray data by *Steck et al.* [2011], might provide further insight.

4. Conclusions

USArray has greatly improved regional data coverage, and despite a very heterogeneous uppermost mantle, there is enough quality *Sn* data to image isotropic *Vp*/*Vs* structure in the mantle lid. However, the *Sn* waveforms are often highly attenuated and emergent and incoherent between stations, which makes accurate picking on two components very difficult. In California, where data coverage generally is best, we found 2θ azimuthal variations for both *Sn-SH* and *Sn-SV* which we cannot convincingly explain. Nevertheless, we favor a joint inversion that includes anisotropic parameters for both *Sn* and *Pn*, with fast axes in the same direction as expected for a hexagonally symmetric material with horizontal symmetry axis. We identify large fast *Vp*/*Vs* anomalies, which can be associated with regions of partial melt in the uppermost mantle, below the Snake River Plain and the Colorado Plateau. Comparing our results to other studies, we find the Snake River Plain anomaly appears consistently from the Moho to depths of about 200 km, whereas the mantle lithosphere below the Colorado Plateau seems to be very heterogeneous. The very low *Pn* velocities below the Sierra

Nevada coincide with a low *Vp*/*Vs* anomaly and can possibly be explained with compositional changes. The Moho depth estimates generally agree with crustal thickness studies from receiver functions, although we find a shallower Moho below the Colorado Plateau.

Acknowledgments
Many thanks to Luciana Astiz for helping with the Antelope system and the ANF seismic analysts and staff for providing the data. We thank the reviewer for constructive comments.

References

Babuska, V., and M. Cara (1991), *Seismic Anisotropy in the Earth*, vol. 10, Kluwer Academic Press, Dordrecht, Netherlands.
Backus, G. E. (1965), Possible forms of seismic anisotropy of the uppermost mantle under oceans, *J. Geophys. Res.*, *70*(14), 3429–3439.
Bakir, A., and R. Nowack (2012), Modeling seismic attributes of Pn waves using the spectral-element method, *Pure Appl. Geophys.*, *169*(9), 1539–1556.
Bath, M. (1978), An analysis of the time term method in refraction seismology, *Tectonophysics*, *51*(3–4), 155–169.
Beghoul, N., M. Barazangi, and B. L. Isacks (1993), Lithospheric structure of Tibet and western North America: Mechanisms of uplift and a comparative study, *J. Geophys. Res.*, *98*(B2), 1997–2016.
Bensen, G., M. Ritzwoller, and Y. Yang (2009), A 3-D shear velocity model of the crust and uppermost mantle beneath the United States from ambient seismic noise, *Geophys. J. Int.*, *177*(3), 1177–1196.
Buehler, J. S., and P. M. Shearer (2010), Pn tomography of the western United States using USArray, *J. Geophys. Res.*, *115*, B09315, doi:10.1029/2009JB006874.
Buehler, J. S., and P. M. Shearer (2012), Localized imaging of the uppermost mantle with USArray Pn data, *J. Geophys. Res.*, *117*, B09305, doi:10.1029/2012JB009433.
Christensen, N. I. (1984), The magnitude, symmetry and origin of upper mantle anisotropy based on fabric analyses of ultramafic tectonites, *Geophys. J. R. Astron. Soc.*, *76*(1), 89–111.
Chulick, G. S., and W. D. Mooney (2002), Seismic structure of the crust and uppermost mantle of North America and adjacent oceanic basins: A synthesis, *Bull. Seismol. Soc. Am.*, *92*(6), 2478–2492, doi:10.1785/0120010188.
Conder, J. A., and D. A. Wiens (2006), Seismic structure beneath the Tonga arc and Lau back-arc basin determined from joint Vp, Vp/Vs tomography, *Geochem. Geophys. Geosyst.*, *7*, Q03018, doi:10.1029/2005GC001113.
Crampin, S. (1981), A review of wave motion in anisotropic and cracked elastic-media, *Wave Motion*, *3*(4), 343–391.
Diaz, J., A. Gil, and J. Gallart (2013), Uppermost mantle seismic velocity and anisotropy in the Euro-Mediterranean region from *Pn* and *Sn* tomography, *Geophys. J. Int.*, *192*(1), 310–325, doi:10.1093/gji/ggs016.
Gilbert, H. (2012), Crustal structure and signatures of recent tectonism as influenced by ancient terranes in the western United States, *Geosphere*, *8*(1), 141–157.
Goes, S., R. Govers, and P. Vacher (2000), Shallow mantle temperatures under Europe from P and S wave tomography, *J. Geophys. Res.*, *105*(B5), 11,153–11,169.
Haines, A. (1980), Differences in time terms between New Zealand seismograph stations and implications for crustal structure, *N. Z. J. Geol. Geophys.*, *23*(5-6), 541–549.
Hearn, T. M. (1996), Anisotropic Pn tomography in the western United States, *J. Geophys. Res.*, *101*(B4), 8403–8414.
Houser, C., G. Masters, P. Shearer, and G. Laske (2008), Shear and compressional velocity models of the mantle from cluster analysis of long-period waveforms, *Geophys. J. Int.*, *174*(1), 195–212, doi:10.1111/j.1365-246X.2008.03763.x.
Ismail, W. B., and D. Mainprice (1998), An olivine fabric database: An overview of upper mantle fabrics and seismic anisotropy, *Tectonophysics*, *296*(1–2), 145–157.
Jones, C. H., H. Kanamori, and S. W. Roecker (1994), Missing roots and mantle and drips: Regional Pn and teleseismic arrival times in the southern Sierra Nevada and vicinity, California, *J. Geophys. Res.*, *99*(B3), 4567–4601.
Jurkevics, A. (1988), Polarization analysis of three-component array data, *Bull. Seismol. Soc. Am.*, *78*(5), 1725–1743.
Keith, C. M., and S. Crampin (1977), Seismic body waves in anisotropic media: Synthetic seismograms, *Geophys. J. R. Astron. Soc.*, *49*(1), 225–243.
Langston, C. A. (1982), Aspects of Pn and Pg propagation at regional distances, *Bull. Seismol. Soc. Am.*, *72*(2), 457–471.
Levander, A., B. Schmandt, M. S. Miller, K. Liu, K. E. Karlstrom, R. S. Crow, C.-T. A. Lee, and E. D. Humphreys (2011), Continuing Colorado plateau uplift by delamination-style convective lithospheric downwelling, *Nature*, *472*(7344), 461–465.
Levin, V., and J. Park (1998), P-SH conversions in layered media with hexagonally symmetric anisotropy: A cookbook, in *Geodynamics of Lithosphere & Earth's Mantle, Pageoph Topical Volumes*, edited by J. Plomerova, R. Liebermann, and V. Babuska, pp. 669–697, Birkhäuser, Basel.
Lin, F.-C., and M. H. Ritzwoller (2011), Helmholtz surface wave tomography for isotropic and azimuthally anisotropic structure, *Geophys. J. Int.*, *186*(3), 1104–1120.
Lin, F.-C., M. H. Ritzwoller, Y. Yang, M. P. Moschetti, and M. J. Fouch (2011), Complex and variable crustal and uppermost mantle seismic anisotropy in the western United States, *Nat. Geosci.*, *4*(1), 55–61.
Liu, K. H. (2009), NA-SWS-1.1: A uniform database of teleseismic shear wave splitting measurements for North America, *Geochem. Geophys. Geosyst.*, *10*, Q05011, doi:10.1029/2009GC002440.
Long, M. D., and T. W. Becker (2010), Mantle dynamics and seismic anisotropy, *Earth Planet. Sci. Lett.*, *297*(334), 341–354.
Lowry, A. R., and M. Perez-Gussinye (2011), The role of crustal quartz in controlling Cordilleran deformation, *Nature*, *471*(7338), 353–357.
Maupin, V., and J. Park (2007), Theory and observations: Wave propagation in anisotropic media, in *Treatise on Geophysics, Seismology and the Structure of the Earth*, vol. 1, edited by B. Romanowicz and A. Dziewonski, pp. 289–321, Elsevier, Amsterdam, Netherlands.
Moschetti, M. P., M. H. Ritzwoller, F. Lin, and Y. Yang (2010a), Seismic evidence for widespread western-US deep-crustal deformation caused by extension, *Nature*, *464*(7290), 885–889.
Moschetti, M. P., M. H. Ritzwoller, F.-C. Lin, and Y. Yang (2010b), Crustal shear wave velocity structure of the western United States inferred from ambient seismic noise and earthquake data, *J. Geophys. Res.*, *115*, B10306, doi:10.1029/2010JB007448.
Nolet, G., C. Coutlee, and R. Clouser (1998), Sn velocities in western and eastern North America, *Geophys. Res. Lett.*, *25*(10), 1557–1560.
Obrebski, M., R. M. Allen, F. Pollitz, and S.-H. Hung (2011), Lithosphere-asthenosphere interaction beneath the western United States from the joint inversion of body-wave traveltimes and surface-wave phase velocities, *Geophys. J. Int.*, *185*(2), 1003–1021.
Park, J., and V. Levin (2002), Seismic anisotropy: Tracing plate dynamics in the mantle, *Science*, *296*(5567), 485–489, doi:10.1126/science.1067319.
Perry, H. K. C., C. Jaupart, J.-C. Mareschal, and N. M. Shapiro (2006), Upper mantle velocity-temperature conversion and composition determined from seismic refraction and heat flow, *J. Geophys. Res.*, *111*, B07301, doi:10.1029/2005JB003921.

Raitt, R. W., G. G. Shor Jr., T. J. G. Francis, and G. B. Morris (1969), Anisotropy of the Pacific upper mantle, *J. Geophys. Res.*, *74*(12), 3095–3109.

Ritzwoller, M., G. Masters, and F. Gilbert (1988), Constraining aspherical structure with low-degree interaction coefficients: Application to uncoupled multiplets, *J. Geophys. Res.*, *93*(B6), 6369–6396.

Ritzwoller, M. H., F.-C. Lin, and W. Shen (2011), Ambient noise tomography with a large seismic array, *C. R. Geosci.*, *343*(8-9), 558–570.

Roth, J. B., M. J. Fouch, D. E. James, and R. W. Carlson (2008), Three-dimensional seismic velocity structure of the northwestern United States, *Geophys. Res. Lett.*, *35*, L15304, doi:10.1029/2008GL034669.

Saleeby, J., and Z. Foster (2004), Topographic response to mantle lithosphere removal in the southern Sierra Nevada region, California, *Geology*, *32*(3), 245–248.

Savage, M. K., and P. G. Silver (1993), Mantle deformation and tectonics: Constraints from seismic anisotropy in the western United States, *Phys. Earth Planet. Inter.*, *78*(334), 207–227.

Schmandt, B., and E. Humphreys (2010), Complex subduction and small-scale convection revealed by body-wave tomography of the western United States upper mantle, *Earth Planet. Sci. Lett.*, *297*(334), 435–445.

Shearer, P., and J. Orcutt (1986), Compressional and shear wave anisotropy in the oceanic lithosphere—The Ngendei seismic refraction experiment, *Geophys. J. Int.*, *87*(3), 967–1003.

Shen, W., M. H. Ritzwoller, and V. Schulte-Pelkum (2013), A 3-D model of the crust and uppermost mantle beneath the Central and western US by joint inversion of receiver functions and surface wave dispersion, *J. Geophys. Res. Solid Earth*, *118*, 262–276, doi:10.1029/2012JB009602.

Soustelle, V., and A. Tommasi (2010), Seismic properties of the supra-subduction mantle: Constraints from peridotite xenoliths from the Avacha volcano, southern Kamchatka, *Geophys. Res. Lett.*, *37*, L13307, doi:10.1029/2010GL043450.

Steck, L. K., M. L. Begnaud, S. Phillips, and R. Stead (2011), Tomography of crustal P and S travel times across the western United States, *J. Geophys. Res.*, *116*, B11304, doi:10.1029/2011JB008260.

Takei, Y. (2002), Effect of pore geometry on VP/VS: From equilibrium geometry to crack, *J. Geophys. Res.*, *107*(B2), 2043, doi:10.1029/2001JB000522.

Tape, C., A. Plesch, J. H. Shaw, and H. Gilbert (2012), Estimating a continuous Moho surface for the California Unified Velocity Model, *Seismol. Res. Lett.*, *83*(4), 728–735, doi:10.1785/0220110118.

Thurber, C. (1993), Local earthquake tomography: Velocities and Vp/Vs-theory, in *Seismic Tomography: Theory and Practice*, edited by H. Iyer and K. Hirahara, pp. 563–583, Chapman and Hall, London.

Tian, Y., and D. Zhao (2012), P-wave tomography of the western United States: Insight into the Yellowstone hotspot and the Juan de Fuca slab, *Phys. Earth Planet. Inter.*, *200–201*, 72–84.

Tryggvason, A., S. T. Rögnvaldsson, and O. G. Flóvenz (2002), Three-dimensional imaging of the P- and S-wave velocity structure and earthquake locations beneath Southwest Iceland, *Geophys. J. Int.*, *151*(3), 848–866.

Wagner, L. S., S. Beck, G. Zandt, and M. N. Ducea (2006), Depleted lithosphere, cold, trapped asthenosphere, and frozen melt puddles above the flat slab in central Chile and Argentina, *Earth Planet. Sci. Lett.*, *245*(12), 289–301.

West, J. D., M. J. Fouch, J. B. Roth, and L. T. Elkins-Tanton (2009), Vertical mantle flow associated with a lithospheric drip beneath the Great Basin, *Nat. Geosci.*, *2*(6), 439–444.

Zhang, H., and C. H. Thurber (2003), Double-difference tomography: The method and its application to the Hayward fault, California, *Bull. Seismol. Soc. Am.*, *93*(5), 1875–1889, doi:10.1785/0120020190.